EDGE ARTICLE

Check for updates

Precise synthesis of telechelic rodlike polyisocyanides: versatile building blocks for fabricating polymer frameworks with controllable pore-apertures

Yang Zong,[a] Run-Tan Gao,[a] Na Liu,*[b] Shixing Lei,[c] Zhan-Ting Li [ID][c] and Zong-Quan Wu [ID] *[a]

The controlled synthesis of telechelic polymers with precisely functionalized chain-ends and predictable main-chain structures is highly desirable. Herein, a series of air-stable *trans*-bis(phenylethynyl)palladium catalysts were designed and efficiently synthesized, which initiate the polymerization of phenyl isocyanides *via* a living chain-growth process, resulting in polyisocyanides with precise control of molecular weights (M_ns) and narrow molecular weight distributions (*Đ*). The substituents of the catalyst can regulate the polymerization rate while serving as entire chain-end functional groups of the resulting polymers. Given the precise control over the length of rigid polyisocyanides, these polyisocyanides are an ideal building block for constructing covalent polymer frameworks (CPF_ms) with tuneable pore apertures and functionalities. As a proof of concept, water-soluble CPFs with tuneable pore-apertures were prepared and the ordering of the resulting CPFs was systematically verified by dynamic light scattering (DLS), high-resolution transmission electron microscopy (HR-TEM), and small-angle X-ray scattering (synchrotron radiation facility). Moreover, the pore aperture can be directly controlled by tuning the length of the polyisocyanide link. Owing to the tuneable pore size and charge attraction effects, the CPFs with pore apertures matching the target single-stranded deoxyribonucleic acid (ssDNA) exhibit good performance on gene delivery. The percentage of delivered ssDNA into cells is up to *ca.* 98% (21 and 35 units).

Introduction

In nature, biological macromolecules such as nucleic acids,[1] polypeptides,[2] and proteins[3] are strictly controlled in terms of their chain length, sequence, and chirality to ensure the accurate transmission of genetic information and the proper execution of biological functions.[4–6] For polymer chemists, the controlled synthesis of polymers is a crucial method for preparing functional materials.[7–9] Benefiting from the development of living polymerization methods, functional polymers with precise structures have found extensive applications in numerous fields, including catalysis,[10,11] drug delivery,[12,13] circularly polarized luminescence and so forth.[14–16] Moreover, to

further modulate the properties of polymers, chain-end functionalization plays a significant role in polymer chemistry.[17,18] By introducing functional chain-end groups, it is not only possible to control the physical properties of polymers, such as the glass transition, but also to endow the polymers with novel characteristics such as multiple stimuli-responsiveness and self-assembly.[19,20] However, due to the influence of the chain length and molecular weight distribution, post-polymerization chain-end functionalization of polymers often faces challenges such as incomplete functionalization, difficult purification, and the need for large excesses of reactive functional groups.[17] Therefore, developing an efficient synthetic method to improve the efficiency of chain-end functionalization is highly necessary. Such polymers have great potential in constructing functional materials, such as amorphous polymer networks and crystalline frameworks, depending on the rigidity of the backbone.

Over the past two decades, porous frameworks have developed rapidly as an important component of functional materials.[21–23] As the special example of porous materials, Omar M. Yaghi and others proposed framework chemistry such as metal–organic frameworks (MOFs), covalent organic

[a]State Key Laboratory of Supramolecular Structure and Materials, College of Chemistry, Jilin University, 2699 Qianjin Street, Changchun, Jilin 130012, China. E-mail: zqwu@jlu.edu.cn

[b]The School of Pharmaceutical Sciences, Jilin University, 1266 Fujin Road, Changchun, Jilin 130021, China. E-mail: liuna606@jlu.edu.cn

[c]State Key Laboratory of Organometallic Chemistry, Shanghai-Hong Kong Joint Laboratory in Chemical Synthesis, Shanghai Institute of Organic Chemistry, University of Chinese Academy of Sciences, Chinese Academy of Sciences, Shanghai 200032, China

frameworks (COFs), supramolecular organic frameworks (SOFs), and hydrogen-bonded organic frameworks (HOFs).[24–30] For porous frameworks, regulating pore size and introducing functional groups are of significant importance for practical applications because they may directly influence molecular accessibility, selectivity, host–guest interactions, and structural stability.[31–33] The pore apertures dictate the size of target molecules that may enter the pores, and provide the surface and space to carry out the functions, such as the storage, separation, and conversion. To precisely control the pore aperture, Yaghi *et al.* synthesized a family of MOFs with pore apertures ranging from 14 to 98 angstroms using organic links containing many phenylene rings.[34] Feng *et al.* constructed a series of COFs with record pore apertures ranging from 7.7 nm to 10.0 nm by using oligomeric ethynylbenzene links.[35] These MOFs and COFs with large pore apertures realized the remarkable application in biomacromolecule encapsulation and separation. Inspired by these studies, controlled synthesis of mesoporous frameworks has a highly promising strategy in protein/gene delivery[36–38] and peptide/protein discrimination.[39,40] In this research area, nucleic acid-based (DNA and RNA) drugs have found applications in various fields, particularly in biomedicine.[41,42] In order to exhibit their pharmacological effect, nucleotide-based drugs should be delivered intracellularly. Nevertheless, the negatively charged and hydrophobic properties of the phospholipid bilayer that forms the cell membrane make this process difficult.[43] Water-soluble cationic polymers efficiently bind and load short nucleic acid chains through size-matching steric effects and electrostatic interactions, and deliver them into cells *via* endocytosis.[44,45] Moreover, the diversity of nucleic acid lengths and species may demand a modular, water-soluble, framework-based delivery platform with facile tunability. However, these frameworks with large pore apertures were usually prepared using long and rigid aromatic linkers, which require multiple and complex organic syntheses and are time-consuming. Moreover, controlling the pore aperture of frameworks with atomic precision has rarely been achieved to date, to the best of our knowledge. Therefore, developing a convenient method for facilely constructing porous frameworks with controllable and large pore apertures in an atomically precise manner is highly desired.

The insertion polymerization of isocyanide gives polyisocyanide with precise control over the chain length and extremely low distribution. Owing to this C1 polymerization, the chain length increased by one carbon atom *via* one monomer insertion, which facilitates atomic control over the chain length. The reported alkyne–Pd(II) catalysts facilitate the controlled synthesis of helical polyisocyanides with controlled molecular weight (M_n) and narrow dispersity ($Đ$).[46–48] The functional Pd(II)-catalysts can afford helical polyisocyanides with a functional group installed on the initiating end, while post-polymerization functionalization can modify the terminating end of polyisocyanide. However, this strategy involves cumbersome and time-consuming experimental efforts, posing a major practical limitation.[49–51]

Controlled synthesis of rodlike helical polyisocyanides bearing functionalities on both chain ends is in great demand, as they can provide useful links for constructing porous frameworks. Herein, we designed and synthesized a class of bis(phenylethynyl)palladium catalysts that can efficiently catalyse living polymerization of various isocyanides, leading to the rodlike stereoregular polyisocyanides with controlled M_ns and narrow $Đ$. The functional phenylethynyl groups of the catalyst were installed at both the initiating and terminating chain ends. Thus, a variety of well-defined end-functionalized polyisocyanides carrying benzene, benzaldehyde, and anisole on each chain end were readily prepared. The benzaldehydes end-functionalized polyisocyanides bearing hydrophilic methyl triglycol on the pendants were used as length-tuneable links for constructing water-soluble covalent polymer frameworks (CPFs) with modulable pore apertures. The periodic structure was undoubtedly confirmed by high-resolution transmission electron microscopy (HR-TEM) and synchrotron small angle X-ray scattering (SAXS). Benefiting from the tuneable pore aperture and electrostatic interactions, these CPFs can accurately recognize ssDNAs of different lengths and achieve efficient delivery into cells, with the percentage of delivered cells reaching up to 98%. Collectively, this study demonstrates that bis(phenylethynyl)palladium catalysts enable the facile synthesis of well-defined helical polyisocyanides with functional groups at both chain ends.

Results and discussion

Synthesis of end-functionalized polyisocyanides

A family of bis(phenylethynyl)palladium catalysts **1a–c** with various substituents at the para position of the benzene ring was synthesized through the reaction of the corresponding phenylethynyl with *trans*-bis(triethyl phosphine)palladium dichloride in dichloromethane using triethylamine as the base at room temperature (Scheme 1 and Fig. S1–S9 in the SI). The resulting Pd(II)-catalysts show excellent solubility in common organic solvents and are air-stable. To assess the catalytic performance of **1a–c**, isocyanide **2a** was employed as a model monomer and was polymerized by **1a** in THF at room temperature ($[2a]_0 = 0.35$ M, $[2a]_0/[Pd]_0 = 75$). However, the polymerization was quite slow, and almost no polymeric product was isolated after 20 h. Then, the polymerization solution was heated to 55 °C. Following overnight polymerization, the solution was directly precipitated into methanol, resulting in a deep yellow solid. The successfully obtained polymer **1a**-poly-**2a**$_{75}$(Pd) (the subscript is the theoretical degree of polymerization (DP)) was characterized by size-exclusion chromatography (SEC), which confirmed its average M_n of 22.6 kg mol^{-1} and a narrow $Đ$ of 1.08 (Fig. 1a). To investigate whether the polymerization exhibited a living character, polymerizations of **2a** catalysed by **1a** with varying $[2a]_0/[Pd]_0$ ratios were conducted. As depicted in Fig. 1a, all the generated **1a**-poly-**2a**$_n$(Pd) polymers exhibited a single-peak SEC distribution and shifted to higher M_n-regions as the $[2a]_0/[Pd]_0$ ratio increased. Moreover, M_n increased linearly with $[2a]_0/[Pd]_0$, and the $Đ$ values for the generated **1a**-poly-**2a**$_n$(Pd)s were less than 1.15 (Fig. 1b), confirming the living nature of the polymerization.
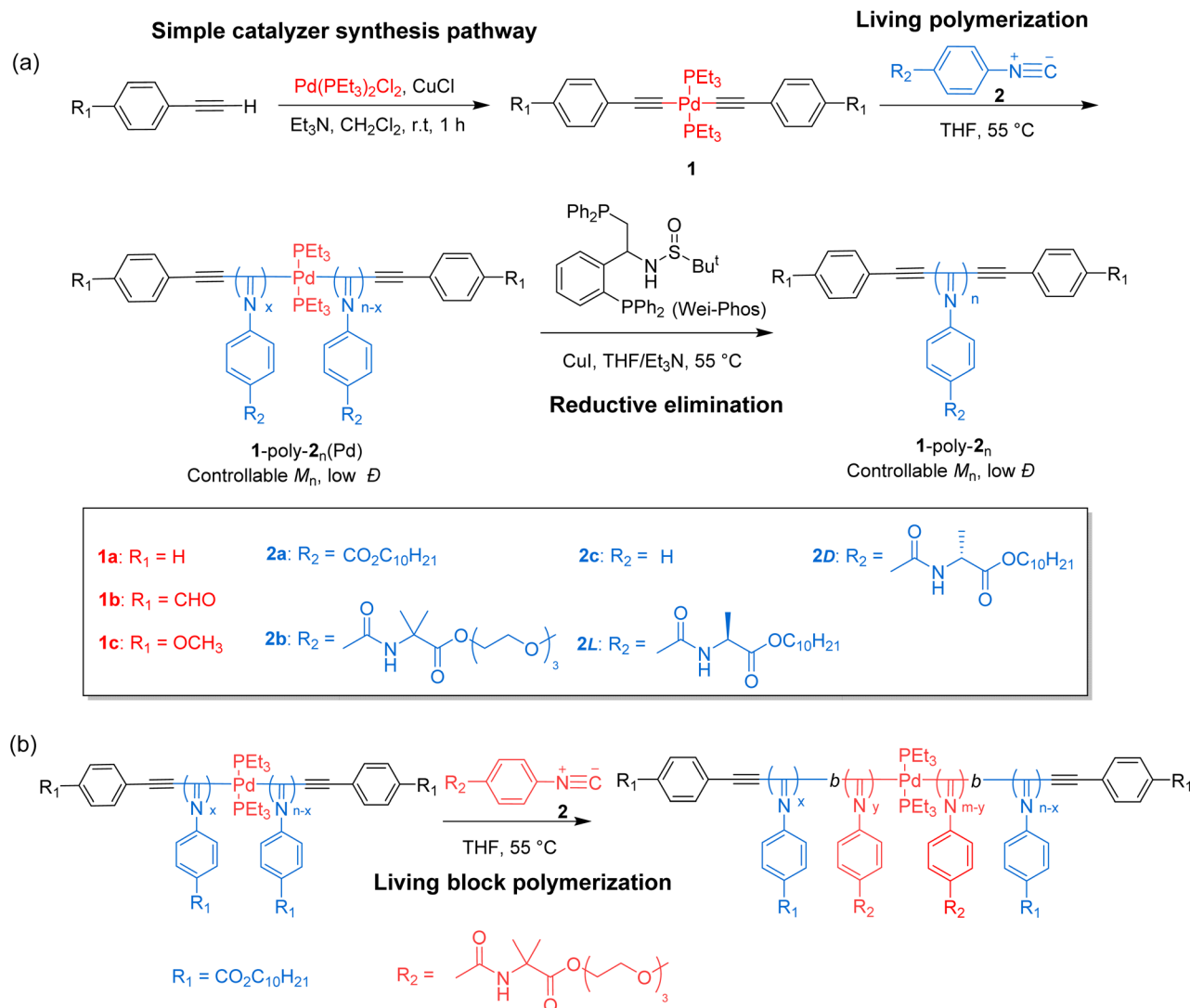
Scheme 1 (a) Synthesis of the catalysts and the living polymerization of isocyanides. (b) Living block polymerization of isocyanides.

Further experiments revealed that catalysts **1b** and **1c** could also catalyze the living polymerization of **2a**, giving the desired polyisocyanides with controlled M_ns and low $Đ$ in high yield. The polymerization process was monitored by analyzing the SEC of aliquots collected at appropriate time intervals to track the changes in the M_n of the resulting polymers and to determine the monomer conversions. The time-dependent SEC for the polymerization of **2a** using **1a**, **1b** and **1c** is summarized in Fig. S10 in the SI. Within four hours, the monomer conversions for the polymerizations catalyzed by **1a**, **1b**, and **1c** are 67%, 51% and 75%, respectively (Fig. 1c). Meanwhile, as shown in Fig. 1d, the plots revealed that the isocyanide polymerizations catalyzed by **1a–c** all follow first-order kinetics, as a clear linear relationship was observed between $-\ln([M]/[M]_0)$ and polymerization time. The apparent polymerization rate constants of the isocyanide polymerization catalyzed by **1a**, **1b**, and **1c** are 7.93×10^{-5}, 4.87×10^{-5}, 9.35×10^{-5} s^{-1}, respectively. That is, the polymerization rate of **2a** using **1c**, carrying an electron-donating (methoxy) substituent, is approximately 1.9 times

higher than that using **1b**, which bears an electron-withdrawing (aldehyde) moiety, indicating that the substituents on the phenylethynyl group of the catalysts influence the polymerization activity. Taking advantage of these catalysts, a variety of telechelic polyisocyanides with different M_n and low $Đ$ were prepared using isocyanide monomers **2a**, **2b**, **2L** and **2D** (Table S1, SI).

The structure and regularity of the isolated polymers were further investigated. The proton nuclear magnetic resonance (^{1}H NMR) spectrum clearly demonstrated the occurrence of polymerization. For instance, the resonances assignable to the terminal benzaldehyde group and the methylene group in the isocyanide side chain were clearly observed in the ^{1}H NMR spectrum of **1b**-poly-**2a**$_{50}$(Pd). The integral ratio of the terminal –C*H*O group to the methylene groups of the pendant is *ca.* 1 : 48, which agrees well with the theoretical DP of 50, further supporting the high controllability of the polymerization (Fig. 2a). The stereoregularity of **1b**-poly-**2a**$_{50}$(Pd) was determined by calculating the half-bandwidth of the main chain imino carbon
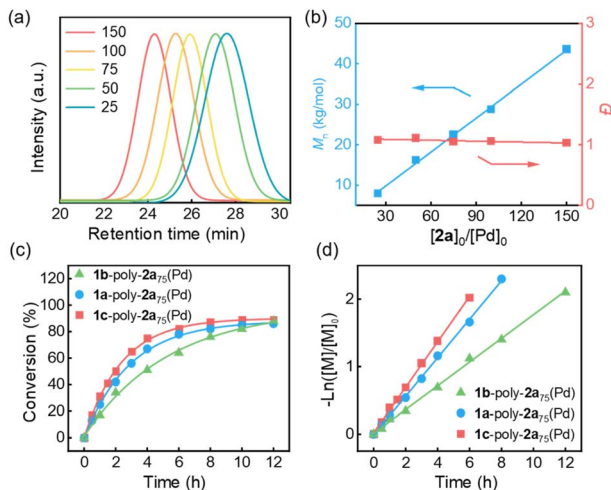
Fig. 1 (a) SEC curves of **1a**-poly-**2a**$_n$(Pd) prepared with different [**2a**]$_0$/[Pd]$_0$ values. (b) Plots of M_ns and $Đ$ values of **1a**-poly-**2a**$_n$(Pd) as a function of [**2a**]$_0$/[Pd]$_0$ values. (c) Plots of **2a** conversion vs. polymerization time of **1**-initiated polymerization of **2a** in THF at 55 °C. (d) First-order kinetic plots for the polymerization of **2a** initiated by **1a**, **1b**, and **1c** in THF at 55 °C ([**2a**]$_0$ = 0.35 M, [**2a**]$_0$/[Pd]$_0$ = 75).
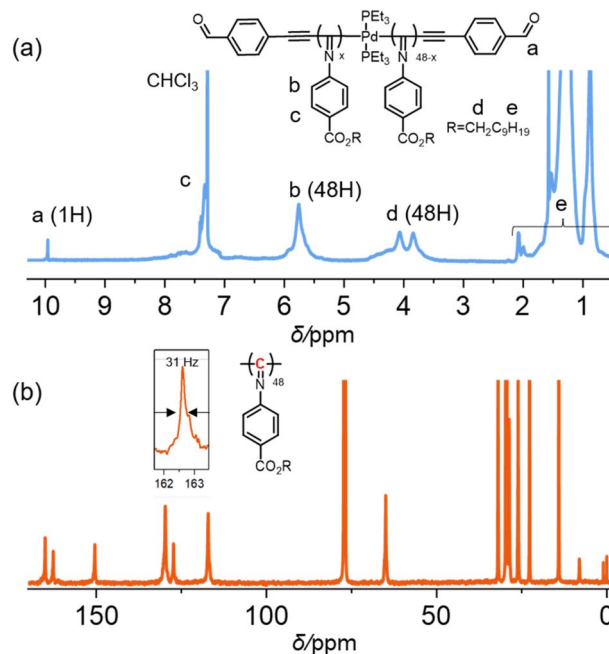
Fig. 2 (a) ^{1}H NMR spectra (500 MHz) and (b) ^{13}C NMR spectra (125 MHz) of **1b**-poly-**2a**$_{50}$(Pd) recorded in CDCl$_3$.

signal in ^{13}C NMR spectra. A rather sharp singlet resonance at δ 162.60 ppm, corresponding to the imino carbons of the polymer backbone, was observed (Fig. 2b). The estimated half-bandwidth was just 31 Hz, suggesting that **1b**-poly-**2a**$_{50}$(Pd) had a high degree of isotactic backbone.[52] The ^{31}P NMR spectrum revealed that **1b**-poly-**2a**$_{50}$(Pd) still retained a metallic palladium moiety (Fig. S11, SI), because the resonance of PEt$_3$ was clearly observed. To further confirm the living nature of the polymerization, a block copolymerization of **2b** with **1a**-poly-**2a**$_{50}$(Pd) (M_n = 16.2 kg mol^{-1}, $Đ$ = 1.11) was conducted in THF at 55 °C ([**2b**]$_0$/[Pd]$_0$ = 15). SEC analysis of the resulting **1a**-poly(**2a**$_{50}$-b-**2b**$_{15}$)(Pd) revealed a monomodal distribution that shifted to a higher M_n-region (Fig. S12, SI). Accordingly, the M_n increased to 21.4 kg mol^{-1} while retaining a low $Đ$ of 1.12. The ^{1}H NMR spectrum of the block copolymer displayed characteristic resonances from both the poly-**2a**$_{50}$ and poly-**2b**$_{15}$ segments (Fig. S13, SI). Integral analysis indicated that the ratio of the poly-**2a**$_{50}$ to poly-**2b**$_{15}$ blocks was 50/13, which is approximately consistent with the feed ratio of the monomers. Furthermore, FT-IR analysis corroborated the formation of the expected block copolymer structure (Fig. S14, SI).

This class of catalysts was also applicable to the polymerization of chiral isocyanide monomers and led to optically active helical polyisocyanides with preferred one-handed helicity. For instance, the polymerization of chiral isocyanide **2L** and **2D** catalyzed by **1b** resulted in helical polyisocyanides **1b**-poly-**2L**$_n$(Pd) and **1b**-poly-**2D**$_n$(Pd), respectively. The excess of one-handed helical sense was assessed by circular dichroism (CD) and UV-vis absorption analyses. The **1b**-poly-**2L**$_n$(Pd) and **1b**-poly-**2D**$_n$(Pd) respectively showed negative and positive CD in the absorption region of the poly(phenyl isocyanide) backbone, indicative of the preferred left- and right-handed helices (Fig. S15, SI).[47] Based on the analyses described above, the

polymerization probably occurred via the isocyanide coordination to the Pd(II) center bound to the phosphine ligand. Subsequently, the monomers underwent ordered insertion at both ends of the palladium center, resulting in the formation of a linear polyisocyanide (Fig. S16, SI). Moreover, the ^{1}H NMR spectrum of the prepared polyisocyanide oligomer **1b**-poly-**2c**$_2$(Pd) with low DP showed simple and symmetric signals, which further confirmed the insertion of isocyanides into both sides of the Pd(II)-center. Due to the living nature of this Pd(II)-initiated polymerization, the initiation process is faster than chain extension, that is, the insertion of isocyanide into Pd–C≡C is easier than into Pd–(C=N–R) (Fig. S17–S20, SI). Thus, the polymerization occurs via the insertion of isocyanides into both sides of the Pd(II)-catalyst.

The Pd(II)-residues embedded in the polymer backbone may have toxic effects on applications related to biology and life sciences. To remove the Pd(II)-residue, the isolated polyisocyanide **1b**-poly-**2a**$_{15}$(Pd) was treated with a bidentate phosphine Wei-Phos (5.0 eq. to Pd) in the presence of triethylamine and cuprous iodide to facilitate the reductive elimination (Scheme 1).[19] It was revealed that the Pd(II)-residue was completely removed, as confirmed by a set of analyses of the resulting polyisocyanides. Prior to the palladium removal reaction, the structural integrity of the synthesized polyisocyanides was investigated by mass spectroscopy (MS). The **1b**-poly-**2a**$_{15}$(Pd) was analyzed by matrix-assisted laser desorption/ionization spectroscopy (MALDI) in combination with time-of-flight (TOF) detection mass spectrometry (MS). It exhibited a maximum peak at 4643.83, corresponding to the molecular weight of 14-mer with integrity terminal benzaldehyde groups and a Pd(PEt$_3$)$_2$ moiety (Fig. 3a). Furthermore, the
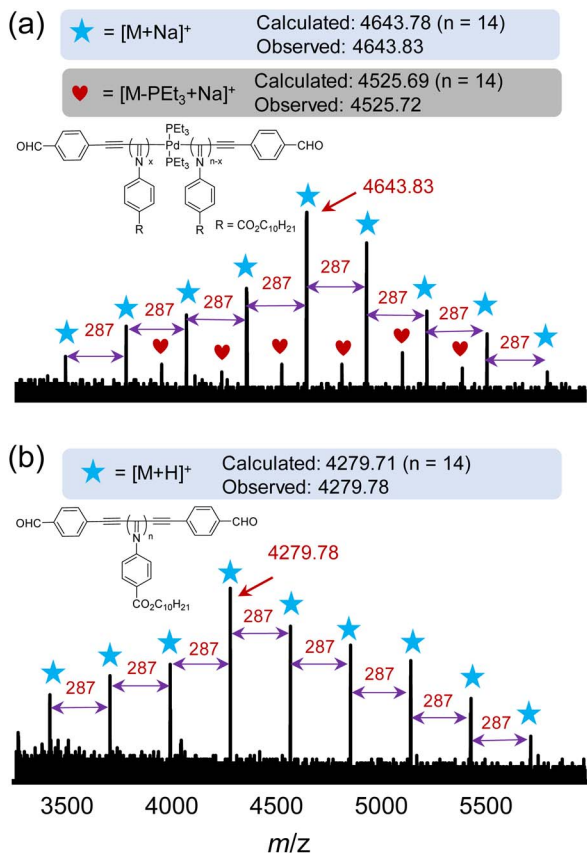
Fig. 3 MALDI-TOF-MS spectra of (a) **1b**-poly-**2a**$_{15}$(Pd) and (b) **1b**-poly-**2a**$_{15}$.

molecular weight difference between adjacent highest peaks is 287, which is equivalent to the molecular weight of a **2a** monomer, indicating the successful insertion of isocyanides. Following the Pd(II)-residue removal reaction, the MALDI-TOF spectrum of **1b**-poly-**2a**$_{15}$ showed the highest peak with an m/z value of 4279.78, corresponding to **1b**-poly-**2a**$_{14}$ (Fig. 3b).

After the reductive elimination of Pd(PEt$_3$)$_2$ from **1b**-poly-**2a**$_{15}$(Pd), the M_n of the resulting **1b**-poly-**2a**$_{15}$ was 4.5 kg mol^{-1}, slightly lower than its precursor (4.7 kg mol^{-1}), while maintaining the narrow distribution with $Đ = 1.08$, as determined by SEC (Fig. 4a). The preservation of the characteristic stretching vibration peaks in the FT-IR spectra of **1b**-poly-**2a**$_{15}$(Pd) and **1b**-poly-**2a**$_{15}$ indicates the structural similarity of the polymer before and after palladium removal (Fig. 4b). No ^{31}P signal could be detected on the ^{31}P NMR spectrum of **1b**-poly-**2a**$_{15}$, suggesting that the Pd(PEt$_3$)$_2$ moiety of **1b**-poly-**2a**$_{15}$(Pd) was clearly removed (Fig. S21, SI). Accordingly, the resonances at 2.01 and 1.26 ppm attributed to the ethyl groups of P(CH$_2$CH$_3$)$_3$ in **1b**-poly-**2a**$_{15}$(Pd) could not be observed in the ^{1}H NMR spectrum of **1b**-poly-**2a**$_{15}$ (Fig. S22, SI). Energy dispersive X-ray spectroscopy (EDS) mapping intuitively showed the disappearance of palladium elements after reductive elimination (Fig. 4c, d, S23 and S24 in SI). Collectively, these studies clearly confirmed the complete removal of the Pd-complex embedded in the polymer backbone. Using this method, a series of
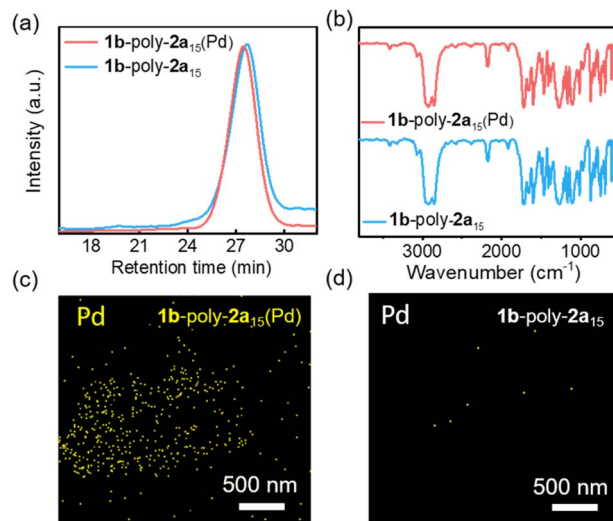

Fig. 4 (a) SEC curves of **1b**-poly-**2a**$_{15}$(Pd) and **1b**-poly-**2a**$_{15}$. (b) FT-IR spectra of **1b**-poly-**2a**$_{15}$(Pd) and **1b**-poly-**2a**$_{15}$ measured at 25 °C using KBr. TEM-EDS elemental mapping images of **1b**-poly-**2a**$_{15}$(Pd) (c) and **1b**-poly-**2a**$_{15}$ (d).

telechelic polyisocyanides, such as **1a**-poly-**2a**$_n$, **1b**-poly-**2a**$_n$, **1c**-poly-**2a**$_n$ and **1a**-poly-**2b**$_n$, with defined chain end functionalities, predictable M_n, and low $Đ$ were facilely prepared (Table S2 and Fig. S25–S30, SI).

Synthesis of CPFs

The acylhydrazone bond, fabricated from the reaction of hydrazine and aldehyde, has been reported as an efficient and convenient dynamic covalent bond in the construction of flexible organic frameworks.[36] To construct water-soluble CPFs,
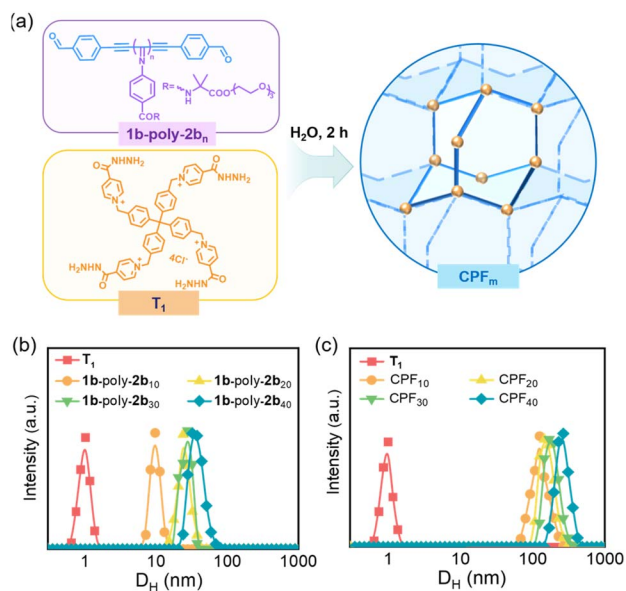

Fig. 5 (a) Synthesis of water-soluble CPF$_m$s. (b) DLS profiles of **T1** (2.0 mM) and **1b**-poly-**2b**$_n$ (0.2 mg mL^{-1}) in water at 25 °C. (c) DLS profiles of **T1** (2.0 mM) and CPF$_m$s (0.2 mg mL^{-1}) in water at 25 °C.

a series of **1b**-poly-**2b**$_n$s with DPs of 10, 20, 30 and 40, were prepared using the method described above (Fig. S31 in SI). The **1b**-poly-**2b**$_n$s of different chain lengths were treated with tetra-armed crosslinker tetrakis-hydrazide **T1** in water while maintaining the stoichiometric ratio of 1 : 2 between the hydrazide groups of **T1** and aldehyde groups of **1b**-poly-**2b**$_n$.[53] The formation of CPFs was monitored by measuring the characteristic signal of CH(OD)$_2$ via ^{1}H NMR spectroscopy of the mixtures at appropriate time intervals. It was revealed that the CH(OD)$_2$ signals completely disappeared within two hours for all the **1b**-poly-**2b**$_n$s, indicating the completion of the reaction of acylhydrazone moiety with benzaldehyde (Fig. 5a, S32 and S33 in the SI).

The dynamic light scattering (DLS) experiment also corroborated the construction of the desired CPF$_m$s. The hydrodynamic diameter (D_H) of **T1** (2.0 mM) is only 0.9 nm, while the D_H values of **1b**-poly-**2b**$_{10}$, **1b**-poly-**2b**$_{20}$, **1b**-poly-**2b**$_{30}$ and **1b**-poly-**2b**$_{40}$, in water (0.2 mg mL^{-1}) were 9.9, 24.0, 27.9, and 33.2 nm, indicative of water soluble macromolecules. However, the D_H values of the resulting CPFs were 125.6, 146.1, 169.9, and 267.2 nm for CPF$_{10}$, CPF$_{20}$, CPF$_{30}$, and CPF$_{40}$, respectively, constructed from **1a**-poly-**2b**$_m$s with DPs of 10, 20, 30, and 40, respectively (Fig. 5b and c). Furthermore, upon varying the concentration of CPF$_{10}$ from 0.1 to 1.5 mg mL^{-1} (Fig. S34, SI), the D_H remained constant, indicating that the D_H of the framework tends to stabilize beyond a certain concentration.

Molecular modeling studies elucidated potential framework configurations of water-soluble CPF$_m$s, where tetrahedral molecule **T1** was employed to form stereoscopic and crosslinking support points, while the rodlike polyisocyanides of varying DPs contributed to the formation of porous frameworks with different pore apertures. The theoretical pore sizes calculated for CPF$_{10}$, CPF$_{20}$, CPF$_{30}$, and CPF$_{40}$ are 8.0, 11.6, 13.3, and 15.1 nm, respectively (Fig. S35, SI). The porous characteristics of these CPF$_m$s were clearly confirmed by HR-TEM observations. As shown in Fig. 6a, the HR-TEM image of CPF$_{10}$ showed distinct square porous structures with a pore aperture of ca. 8.4 nm. As the DPs of the links increased, the HR-TEM image of CPF$_{20}$ also showed a periodic square pore structure, and the pore aperture was increased to ca. 10.5 nm (Fig. 6b). For CPF$_{30}$ and CPF$_{40}$, with further increased pore sizes, the square pore structure could not be observed on HR-TEM images; however, the clear lattice fringes were observed. The pore apertures of CPF$_{30}$ and CPF$_{40}$ were estimated to be 14.6 nm and 16.7 nm, respectively (Fig. S36, SI). As the DP of **1b**-poly-**2b**$_m$s increases, the enlargement of pore apertures makes the maintenance of CPFs more challenging, while the rigid structure of polyisocyanides stabilizes the framework structure. Interestingly, the pore aperture determined by HR-TEM was linearly correlated to the DP of the polyisocyanide links (Fig. 6c). The ordering of the CPF$_m$s of different pore apertures was further verified via synchrotron SAXS analysis. The water solution-phase synchrotron SAXS curves of CPF$_{10}$ and CPF$_{20}$ exhibit peaks at $q \approx 0.76$ and 0.54 nm, respectively, which correspond to the {100} peak and indicate pore apertures of 8.27 nm for CPF$_{10}$ and 11.64 nm for CPF$_{20}$, closely agreeing with the HR-TEM observations (Fig. 6d and e).

Similarly, CPF$_{30}$ and CPF$_{40}$ exhibit peaks at $q \approx 0.44$ and 0.39 nm on the SAXS profiles, corresponding to the pore apertures of 14.28 and 16.11 nm, respectively (Fig. S37, SI), generally
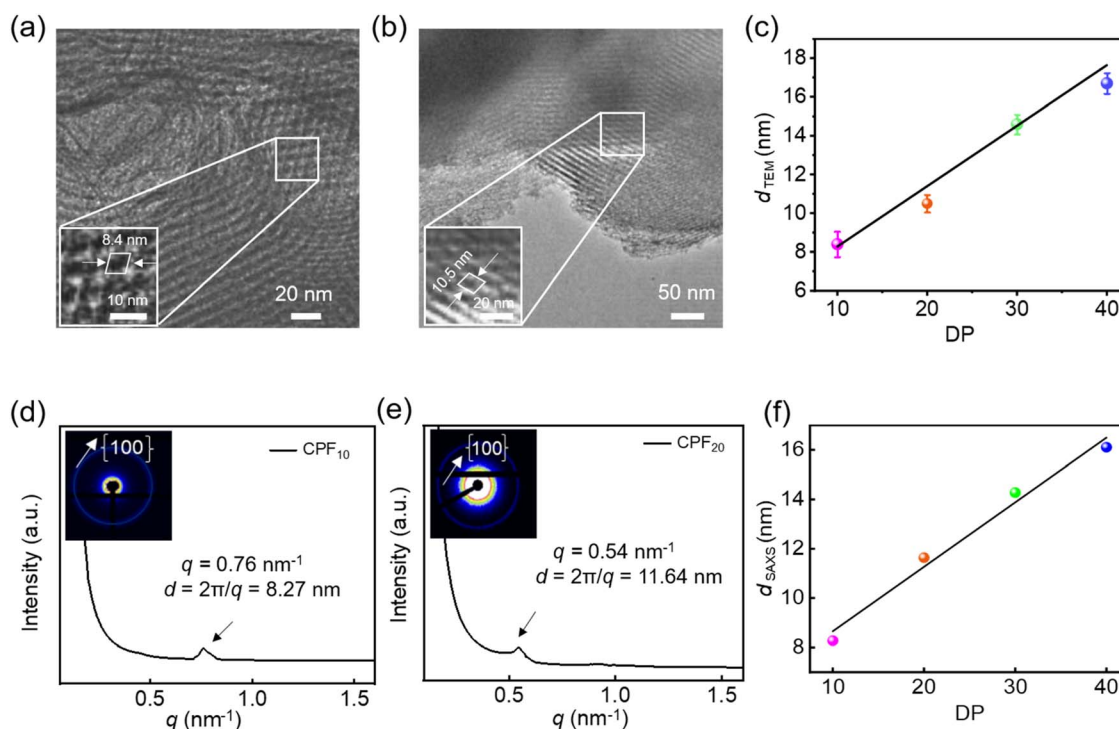

Fig. 6 HR-TEM images of CPF$_{10}$ (a) and CPF$_{20}$ (b). (c) Plot of d-spacing (TEM) vs. the DP of the polyisocyanide link. Solution-phase synchrotron SAXS profiles of CPF$_{10}$ (d) and CPF$_{20}$ (e) recorded in H$_2$O (10 mg mL^{-1}). (f) Plot of d-spacing (SAXS) vs. the DP of the polyisocyanide link.
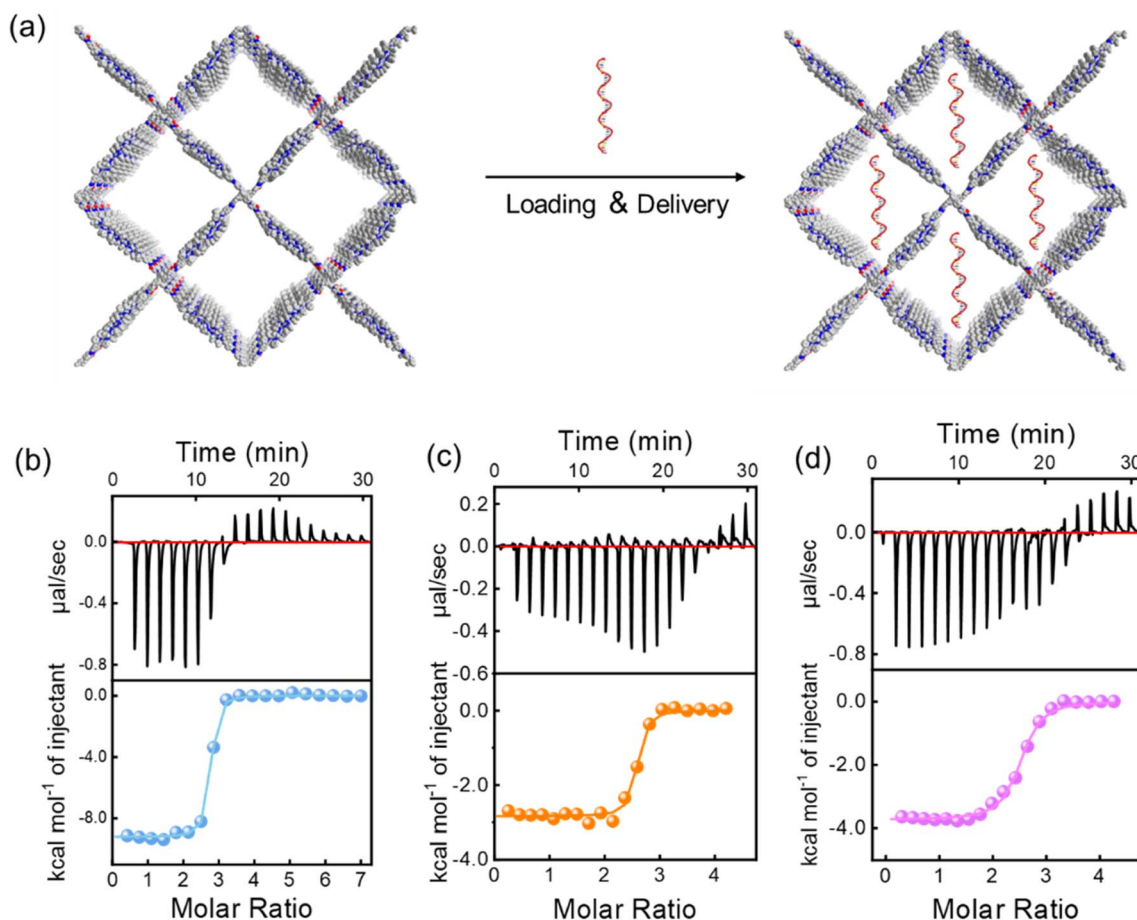
Fig. 7 (a) Schematic representation of the *in situ* loading of ssDNAs into CPF$_m$s. (b–d) Isothermal titration thermograms of CPF$_m$s titrated by ssDNAs (b and c) and ssDNA35 (d) into the solution of CPF$_{10}$ (b), CPF$_{20}$ (c) and CPF$_{30}$ (d) at 25 °C in H$_2$O ([anion] = 0.1 mM; [cation] = 50 μmol). [Anion] represents the total phosphate concentration of the ssDNAs. [Cation] represents the total pyridinium concentration of CPFs. The solid lines represent the best nonlinear fit of the data to a 1 : 1 binding mode.

constant with the HR-TEM observations. It is worth noting that the pore aperture of the constructed frameworks was linearly correlated to the length of the 1b-poly-2b$_m$ links (Fig. 6f). Since the length of 1b-poly-2b$_m$ was determined by the DP of the backbone, it can be facilely controlled by tuning the initial feed ratio of the isocyanide monomer to the catalyst. Thus, the pore aperture of the CPF$_m$s is precisely controllable.

DNA delivery

Based on the successful preparation of water-soluble CPF$_m$s with controlled pore apertures, we explored their application for DNA delivery. The isothermal titration calorimetry (ITC) experiments were first conducted *in vitro* to test the interaction between CPF$_m$s and ssDNA of 21 and 35 units (ssDNA21 and ssDNA35) (Fig. 7a). As depicted in Table 1, the encompassed thermodynamic information, such as the stoichiometry (N), apparent binding constants (K_a), enthalpy change (ΔH), and entropy change (ΔS), was summarized. Given the complexity of DNA-CPF$_m$s binding in real

Table 1 Thermodynamic parameters for the binding of ssDNAs with CPF$_m$s in H$_2$O at 25 °C measured by ITC

DNA	CPF$_m$	K_a (M^{-1})	ΔH (kcal mol^{-1})	$-T\Delta S$ (kcal mol^{-1})	ΔG (kcal mol^{-1})
ssDNA21	CPF$_{10}$	$(2.28 \pm 0.46) \times 10^7$	-6.19 ± 0.055	-8.94	-15.13 ± 0.055
	CPF$_{20}$	$(1.59 \pm 0.66) \times 10^7$	-2.84 ± 0.039	-7.01	-9.85 ± 0.039
	CPF$_{30}$	$(1.36 \pm 0.22) \times 10^7$	-4.14 ± 0.026	-5.60	-9.74 ± 0.026
	CPF$_{40}$	$(4.29 \pm 0.90) \times 10^6$	-2.83 ± 0.029	-6.23	-9.06 ± 0.029
ssDNA35	CPF$_{10}$	$(1.37 \pm 0.34) \times 10^6$	-3.91 ± 0.065	-4.50	-8.41 ± 0.065
	CPF$_{20}$	$(2.47 \pm 0.26) \times 10^6$	-3.74 ± 0.043	-4.71	-8.45 ± 0.043
	CPF$_{30}$	$(3.63 \pm 0.42) \times 10^6$	-9.37 ± 0.202	-0.82	-10.19 ± 0.202
	CPF$_{40}$	$(1.54 \pm 0.26) \times 10^6$	-3.97 ± 0.047	-4.50	-8.47 ± 0.047
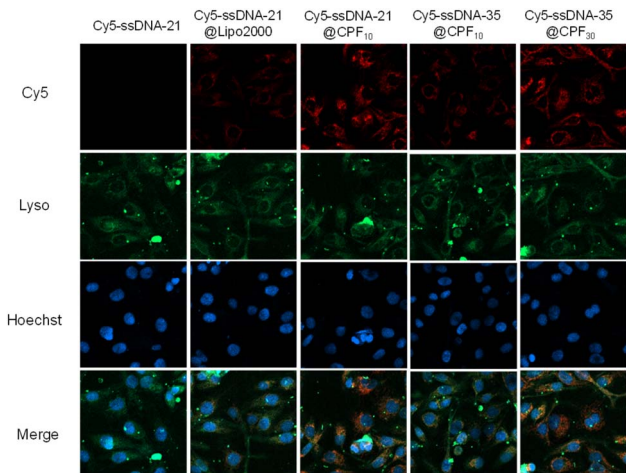
Fig. 8 CLSM images of H9C2 cells after incubation for 2 h with Cy5-ssDNA21, Cy5-ssDNA21@Lipo2000, Cy5-ssDNA21@CPF$_{10}$, Cy5-ssDNA35@CPF$_{10}$, and Cy5-ssDNA35@CPF$_{30}$. The dosages of Cy5-ssDNA21 and Cy5-ssDNA35 were 2.5 μg mL^{-1}, while those of Lipo2000, CPF$_{10}$ and CPF$_{30}$ were 15 μg mL^{-1}. Nuclei and lysosomes were stained with Hoechst (blue) and Lyso-Tracker Green (green), respectively.

scenarios, a 1 : 1 binding model was adopted in ITC to simplify the analysis and ensure comparability with existing literature.[43] Assuming each CPF$_m$s aperture exhibited uniform binding affinity to one entire ssDNA, the K_a values can be calculated.[44] In the binding interaction between CPF$_m$s and ssDNAs in H$_2$O, the K_a values are quite high and varying from 1.37×10^6 to 2.28×10^7 M^{-1} in H$_2$O depending on the pore aperture of CPF$_m$s (Table 1 and Fig. 7b–d). In contrast, the binding between the individual **T1** and the linear polymer **1b**-poly-**2b**$_{10}$ with Cy5-ssDNA was negligible as revealed by ITC analysis (Fig. S38–S40, SI).

The experimental results also indicate that CPF$_m$s with different pore apertures have varying binding strengths with ssDNA, suggesting that the size-matching effect plays a crucial role in the binding. In all instances of CPF$_m$ binding to ssDNA, the entire binding process of ssDNA is a spontaneous behavior driven by both entropy and enthalpy, where the enthalpy contribution is likely primarily due to electrostatic interactions

between ion pairs, and the entropy contribution is likely mainly due to the release of high-energy water to lower the freedom from the hydrophobic surfaces.

The above ITC experiments confirmed the binding affinity of the CPF$_m$s toward ssDNA21 and ssDNA35. Among them, CPF$_{10}$ and CPF$_{30}$ demonstrated remarkably high binding affinity and have great potential for ssDNA delivery. Subsequently, confocal laser scanning microscopy (CLSM) was employed to evaluate the capacity of CPF$_{10}$ and CPF$_{30}$ for delivering Cy5-ssDNA21 and Cy5-ssDNA35 into H9C2 cells (Fig. 8).

The lysosomes and nuclei of the cells were labeled with Lyso-Tracker Green and Hoechst dye, respectively, and were post-incubated with Cy5-ssDNA21 (2.5 μg mL^{-1}) and its *in situ* combinations with CPF$_{10}$ and CPF$_{30}$ for 2 h together; all imagery was captured. For comparative purposes, CPF$_m$s remained constant at 15 μg mL^{-1} across all variations. At the same time, the commercial reagent Lipo2000 was evaluated for its ssDNA delivery efficacy at an equivalent concentration, serving as a positive control. In the presence of the CPF$_m$s, fluorescence of the Cy5 probe was evident in all images, with Cy5-ssDNA21@CPF$_{10}$ and Cy5-ssDNA35@CPF$_{30}$ exhibiting more intense fluorescence. Conversely, in the absence of CPF$_m$s, no fluorescence signal from the Cy5 dye was detected, suggesting that due to the barrier imposed by the cell membrane, Cy5-ssDNA21 alone cannot be delivered into the cells. Under identical incubation times and dosages, weak fluorescence of Cy5 within the cells was observed with Lipo2000, indicating uneven delivery and low delivery efficiency. Compared to the commercial reagent Lipo2000, CPF$_m$s demonstrate superior delivery efficiency for Cy5-ssDNA. The CPF$_m$s with different pore sizes exhibit a size-matching effect with ssDNAs of varying chain lengths, which correlates with the binding affinity determined by ITC (Table 1). Additionally, the fluorescence signals of Cy5 dye and lysosome-stained Lyso-Tracker Green were significantly co-localized, verifying that Cy5-ssDNA21 and Cy5-ssDNA35 were internalized *via* endocytosis facilitated by CPF$_{10}$ and CPF$_{30}$ delivery. Conversely, no co-localization was detected between the Cy5 and Hoechst dyes, suggesting that CPF$_m$s did not transport DNA into cell nuclei within a 2 h incubation period.
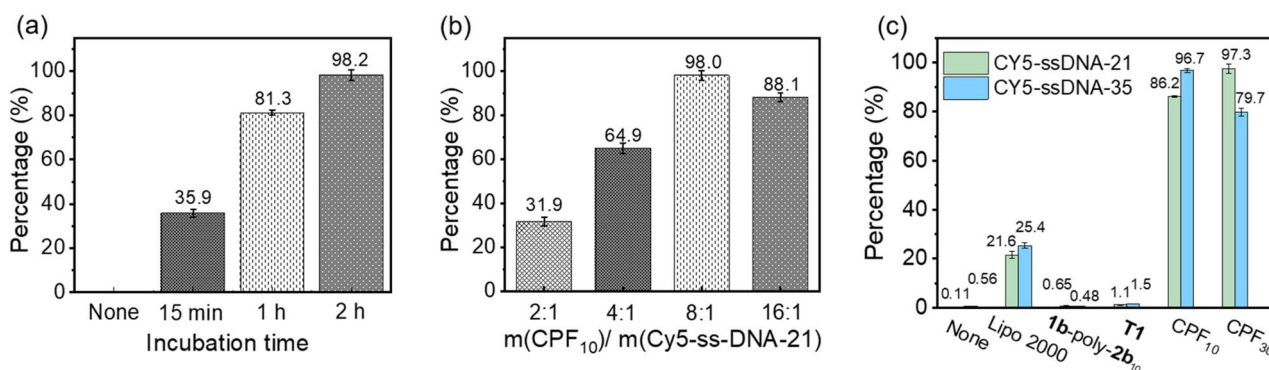
Fig. 9 The efficiency of delivering Cy5-ssDNA21 (2.5 μg mL^{-1}) to H9C2 cells with CPF$_{10}$ as a carrier under different (a) incubation times and (b) experimental dosages. (c) Delivery of Cy5-ssDNA21 and Cy5-ssDNA35 (2.5 μg mL^{-1}) into H9C2 cells by none, Lipo2000 (20 μg mL^{-1}), **1b**-poly-**2b**$_{10}$ (20 μg mL^{-1}), **T1** (20 μg mL^{-1}), CPF$_{30}$ (20 μg mL^{-1}) and CPF$_{10}$ (20 μg mL^{-1}) after incubation for 2 h.

Since the CLSM imaging experiments confirmed that CPF_{10} and CPF_{30} could effectively deliver Cy5-ssDNA21 and Cy5-ssDNA35 into cells, flow cytometry experiments were conducted to quantitatively assess their delivery capabilities. Cy5-ssDNA21 and CPF_{10} were used as preliminary examples to screen the incubation time in H9C2 cells. The percentage of cells that underwent DNA internalization was recorded to determine the optimal incubation time. The percentage of cells undergoing internalization increased with extended incubation time, reaching 35.9%, 81.3%, and 98.2% for 0.25, 1 and 2 h, respectively (Fig. 9a). A similar screening of the CPF_ms and DNA delivery ratios determined the optimal delivery mass ratio to be 8 : 1, indicating that the corresponding CPF_m concentration for ssDNA21 (20 μg mL^{-1}) delivery is 2.5 μg mL^{-1} (Fig. 9b). Note that lacking any delivery agent or only in the presence of **1b**-poly-$2b_n$, the precursor of CPF_ms, Cy5-ssDNA21 showed a poor internalization percentage (<2%), which again confirmed the necessity of a complete CPF_ms delivery vehicle. With CPF_{10} and CPF_{30} as the delivery agents, they demonstrated high delivery efficiency for both Cy5-ssDNA21 and Cy5-ssDNA35. Specifically, CPF_{10}, with a smaller pore aperture, achieved an internalization efficiency of 96.7% for Cy5-ssDNA21 and 86.2% for Cy5-ssDNA35, respectively. In contrast, CPF_{30} with a larger pore aperture exhibited increased delivery trends, with an internalization percentage of 97.3% for Cy5-ssDNA35 and 79.7% for Cy5-ssDNA21. Compared to the commercial reagent Lipo2000, CPF_{10} and CPF_{30} both showed more than a threefold increase in delivery efficiency under the same experimental conditions (Fig. 9c and S41–S44 in the SI).

Conclusion

In summary, this work conveniently synthesized a class of air-stable bis(phenylethynyl)palladium catalysts, which can efficiently catalyze living insertion polymerization of various isocyanides. The resulting well-defined polyisocyanides possess controlled M_n and narrow $Đ$ and bear intact chain-end functionalities. The activity of the Pd(II)-catalysts can be simply modulated by varying the substituents. Importantly, the Pd(II)-complex embedded in the polymer backbone can be easily removed *via* reductive elimination. Interestingly, owing to the rigid rodlike backbone, precisely controlled chain length, and relatively narrow distribution, these well-defined polyisocyanides were utilized to construct porous polymer frameworks with tunable pore structures. The polyisocyanides bearing benzaldehyde on each chain end reacted with a four-arm linker **T1**, affording a class of CPF_ms with ordered structures and tunable pore apertures, as confirmed by DLS, HR-TEM, and SAXS. The pore apertures increase progressively with the DP of the polyisocyanide backbone, indicative of pore-size controllability. The water-soluble CPF_ms were further employed for the delivery of ssDNA21 and ssDNA35 into H9C2 cells. The achieved delivery efficiency was up to 98%, which is more than three times higher than that of the commercial reagent Lipo2000. The present study developed a new kind of catalyst for the precise synthesis of well-defined telechelic polymers, which have great potential in the construction of ordered porous frameworks with tunable pore structures. In the future, by modulating the framework aperture and the functional groups of polyisocyanide pendants, it has the potential to become a versatile platform for the loading of biomacromolecules, enabling a variety of biological applications. Simultaneously, through the alteration of catalyst substituents, it holds promise as a universal link for constructing other porous materials and molecular cages.

Author contributions

Z.-Q. W., N. L., and Z.-T. L. designed and directed the project, Y. Z., R.-T. G., and S. L. performed the experiments and analyzed the data. Z.-Q. W., N. L., and Y. Z. wrote the manuscript with input from all other authors.

Conflicts of interest

There are no conflicts to declare.

Data availability

The data that support the findings of this study are available in the supplementary information (SI) of this article. Supplementary information: experimental details and additional spectra. See DOI: **https://doi.org/10.1039/d5sc07130e**.

Acknowledgements

Notes and references

1 R. Kumar, C. F. S. Chalarca, M. R. Bockman, C. V. Bruggen, C. J. Grimme, R. J. Dalal, M. G. Hanson, J. K. Hexum and T. M. Reineke, *Chem. Rev.*, 2021, **121**, 11527–11652.

2 W. Zhao, Y. Lv, J. Li, Z. Feng, Y. Ni and N. Hadjichristidis, *Angew. Chem., Int. Ed.*, 2021, **60**, 889–895.

3 R. E. Thompson and T. W. Muir, *Chem. Rev.*, 2020, **120**, 3051–3126.

4 M. J. Lajoie, A. J. Rovner, D. B. Goodman, H.-R. Aerni, A. D. Haimovich, G. Kuznetsov, J. A. Mercer, H. H. Wang, P. A. Carr, J. A. Mosberg, N. Rohland, P. G. Schultz, J. M. Jacobson, J. Rinehart, G. M. Church and F. J. Isaacs, *Science*, 2013, **342**, 357–360.

5 R. Hu, J. Wang, A. J. Qin and B. Z. Tang, *Biomacromolecules*, 2022, **23**, 2185–2196.

6 H. Almeida, G. Traverso, B. Sarmento and J. das Neves, *Nat. Rev. Bioeng.*, 2024, **2**, 609–625.

7 D. A. Corbin and G. M. Miyake, *Chem. Rev.*, 2022, **122**, 1830–1874.

8 T. Aida, E. W. Meijer and S. I. Stupp, *Science*, 2012, **335**, 813–817.

9 Y. Song, Y. Kim, Y. Noh, V. K. Singh, S. K. Behera, A. Abudulimu, K. Chung, R. Wannemacher, J. Gierschner, L. Lüer and M. S. Kwon, *Macromolecules*, 2019, **52**, 5538–5545.

10 Y. Yoshinaga, T. Yamamoto and M. Suginome, *J. Am. Chem. Soc.*, 2020, **142**, 18317–18323.

11 Y. Yoshinaga, T. Yamamoto and M. Suginome, *ACS Macro Lett.*, 2017, **6**, 705–710.

12 M. A. van Dongen, C. A. Dougherty and M. M. Banaszak Holl, *Biomacromolecules*, 2014, **15**, 3215–3234.

13 M. A. Beach, U. Nayanathara, Y. Gao, C. Zhang, Y. Xiong, Y. Wang and G. K. Such, *Chem. Rev.*, 2024, **124**, 5505–5616.

14 B. H. Liu, Y. Zong, N. Liu and Z.-Q. Wu, *Sci. China: Chem.*, 2024, **67**, 3247–3257.

15 S. Ma, J. Jiang, Z. Liu, Y. Jiang, Z. Wu and M. Liu, *Nanoscale*, 2020, **12**, 7895–7901.

16 D. Yang, P. Duan, L. Zhang and M. Liu, *Nat. Commun.*, 2017, **8**, 15727.

17 J. Kim, H. Y. Jung and M. J. Park, *Macromolecules*, 2020, **53**, 746–763.

18 S. Pispas and N. Hadjichristidis, *Macromolecules*, 1994, **27**, 1891–1896.

19 X.-H. Xu, W.-B. Liu, X. Song, L. Zhou, N. Liu, Y.-Y. Zhu and Z.-Q. Wu, *Polym. Chem.*, 2021, **12**, 4838–4845.

20 R.-T. Gao, S.-Y. Li, Y. Zong, Z. Chen, N. Liu and Z.-Q. Wu, *Angew. Chem., Int. Ed.*, 2024, **63**, e202410010.

21 X.-H. Xu, Y.-X. Li, L. Zhou, N. Liu and Z.-Q. Wu, *Chem. Sci.*, 2022, **13**, 1111–1118.

22 W. Song, Y. Zhang, C. H. Tran, H. K. Choi, D.-G. Yu and I. Kim, *Prog. Polym. Sci.*, 2023, **142**, 101691.

23 S. Kitagawa, *Acc. Chem. Res.*, 2017, **50**, 514–516.

24 O. M. Yaghi, *J. Am. Chem. Soc.*, 2016, **138**, 15507–15509.

25 R. Freund, O. Zaremba, G. Arnauts, R. Ameloot, G. Skorupskii, M. Dincă, A. Bavykina, J. Gascon, A. Ejsmont, J. Goscianska, M. Kalmutzki, U. Lachelt, E. Ploetz, C. S. Diercks and S. Wuttke, *Angew. Chem., Int. Ed.*, 2021, **60**, 23975–24001.

26 S. D. Diwakara, W. S. Ong, Y. H. Wijesundara, R. L. Gearhart, F. C. Herbert, S. G. Fisher, G. T. McCandless, S. B. Alahakoon, J. J. Gassensmith, S. C. Dodani and R. A. Smaldone, *J. Am. Chem. Soc.*, 2022, **144**, 2468–2473.

27 B. Wang, R.-B. Lin, Z. Zhang, S. Xiang and B. Chen, *J. Am. Chem. Soc.*, 2020, **142**, 14399–14416.

28 K.-D. Zhang, J. Tian, D. Hanifi, Y. Zhang, A. C.-H. Sue, T.-Y. Zhou, L. Zhang, X. Zhao, Y. Liu and Z.-T. Li, *J. Am. Chem. Soc.*, 2013, **135**, 17913–17918.

29 B. Han, H. Wang, C. Wang, H. Wu, W. Zhou, B. Chen and J. Jiang, *J. Am. Chem. Soc.*, 2019, **141**, 8737–8740.

30 M. Zhao, Y. Huang, Y. Peng, Z. Huang, Q. Ma and H. Zhang, *Chem. Soc. Rev.*, 2018, **47**, 6267–6295.

31 A. Thomas, *Angew. Chem., Int. Ed.*, 2010, **49**, 8328–8344.

32 Y. Yuan and G. Zhu, *ACS Cent. Sci.*, 2019, **5**, 409–418.

33 Y. Gu, J. Zhao and J. A. Johnson, *Angew. Chem., Int. Ed.*, 2020, **59**, 5022–5049.

34 H. Deng, S. Grunder, K. E. Cordova, C. Valente, H. Furukawa, M. Hmadeh, F. Gandara, A. C. Whalley, Z. Liu, S. Asahina, H. Kazumori, M. O'Keeffe, O. Terasaki, J. F. Stoddart and O. M. Yaghi, *Science*, 2012, **336**, 1018–1023.

35 Z. Mu, Y. Zhu, B. Li, A. Dong, B. Wang and X. Feng, *J. Am. Chem. Soc.*, 2022, **144**, 5145–5154.

36 J.-L. Lin, Z.-K. Wang, Z.-Y. Xu, L. Wei, Y.-C. Zhang, H. Wang, D.-W. Zhang, W. Zhou, Y.-B. Zhang, Y. Liu and Z.-T. Li, *J. Am. Chem. Soc.*, 2020, **142**, 3577–3582.

37 X. Chen, Q. Zheng, W. Cai, J. Sheng and M. Wang, *ACS Appl. Mater. Interfaces*, 2023, **15**, 54346–54352.

38 Z.-T. Li, S.-B. Yu, Y. Liu, J. Tian and D.-W. Zhang, *Acc. Chem. Res.*, 2022, **55**, 2316–2325.

39 S. Yu, F. Lin, J. Tian, J. Yu, D. Zhang and Z.-T. Li, *Chem. Soc. Rev.*, 2022, **51**, 434–449.

40 Y. Li, Q. Li, X. Miao, C. Qin, D. Chu and L. Cao, *Angew. Chem., Int. Ed.*, 2021, **60**, 6744–6751.

41 X. Tan, F. Jia, P. Wang and K. Zhang, *J. Controlled Release*, 2020, **323**, 240–252.

42 X. Tan, B. B. Li, X. Lu, F. Jia, C. Santori, P. Menon, H. Li, B. Zhang, J. J. Zhao and K. Zhang, *J. Am. Chem. Soc.*, 2015, **137**, 6112–6115.

43 Z. Wang, J. Lin, Y. Zhang, C. Yang, Y. Zhao, Z. Leng, H. Wang, D. Zhang, J. Zhu and Z.-T. Li, *Mater. Chem. Front.*, 2021, **5**, 869–875.

44 B. Yang, X. Zhang, J. Li, J. Tian, Y. Wu, F. Yu, R. Wang, H. Wang, D. Zhang, Y. Liu, L. Zhou and Z.-T. Li, *CCS Chem.*, 2019, **1**, 156–165.

45 B. Shi, M. Zheng, W. Tao, R. Chung, D. Jin, D. Ghaffari and O. C. Farokhzad, *Biomacromolecules*, 2017, **18**, 2231–2246.

46 Y.-X. Xue, Y.-Y. Zhu, L.-M. Gao, X.-Y. He, N. Liu, W.-Y. Zhang, J. Yin, Y. Ding, H. Zhou and Z.-Q. Wu, *J. Am. Chem. Soc.*, 2014, **136**, 4706–4713.

47 N. Liu, L. Zhou and Z.-Q. Wu, *Acc. Chem. Res.*, 2021, **54**, 3953–3967.

48 N. Liu, R.-T. Gao and Z.-Q. Wu, *Acc. Chem. Res.*, 2023, **56**, 2954–2967.

49 K. Onitsuka, M. Yamamoto, T. Mori, F. Takei and S. Takahashi, *Organometallics*, 2006, **25**, 1270–1278.

50 K. Onitsuka, K.-I. Yabe, N. Ohshiro, A. Shimizu, R. Okumura, F. Takei and S. Takahashi, *Macromolecules*, 2004, **37**, 8204–8211.

51 A. Croom, R. Tarallo and M. Weck, *J. Polym. Sci., Part A: Polym. Chem.*, 2016, **54**, 2766–2773.

52 M. M. Green, R. A. Gross, F. C. Schilling, K. Zero and C. Crosby, *Macromolecules*, 1988, **21**, 1839–1846.

53 J.-D. Sun, Q. Li, W.-W. Haoyang, D.-W. Zhang, H. Wang, W. Zhou, D. Ma, J.-L. Hou and Z.-T. Li, *Mol. Pharmaceutics*, 2022, **19**, 953–962.